

NPOI observations of double stars Mizar A and Matar

C.A. Hummel¹, D. Mozurkewich², J.T. Armstrong²,

Arsen R. Hajian¹, N.M. Elias II^{1,3}, D.J. Hutter¹

Electronic mail: cah@fornax.usno.navy.mil, mozurk@rsd.nrl.navy.mil,

tarmstr@fornax.usno.navy.mil, hajian@fornax.usno.navy.mil,

nme@sextans.lowell.edu, djh@fornax.usno.navy.mil

Received _____; accepted _____

To be submitted to the Astronomical Journal

¹Astrometry Department, U.S. Naval Observatory, 3450 Massachusetts Avenue NW,
Washington, DC 20392

²Remote Sensing Division, Naval Research Laboratory, 4555 Overlook Av SW,
Washington, DC 20375

³Mailing address: US Naval Observatory, P.O. Box 1149, Flagstaff, AZ 86002

ABSTRACT

We present a detailed analysis of two spectroscopic binaries based on new observations obtained with the Navy Prototype Optical Interferometer (NPOI). While the data calibration needs refinement, first results show the impressive potential of NPOI, both in terms of speed and precision, for imaging and modeling the orbits of spectroscopic binaries. We determine the orbital parameters of Mizar A (ζ^1 Ursae Majoris) and Matar (η Pegasi), and derive masses and luminosities using published radial velocities and Hipparcos trigonometric parallaxes. The results on Mizar A are compared to earlier work done with the Mark III interferometer, while data from this instrument were combined with NPOI data in the Matar analysis.

Subject headings: techniques : interferometric — binaries: spectroscopic

1. Introduction and outline

In recent years, a new class of optical interferometers with very long baselines and more than two elements has promised to image stars and stellar systems with unprecedented resolution and accuracy (see the review by Armstrong *et al.* 1995). One of these, the Navy Prototype Optical Interferometer (NPOI), near Flagstaff, Arizona, has been described in detail by Armstrong *et al.* (1998), and first results were presented by Benson *et al.* (1997) and Hajian *et al.* (1998). Among the scientific goals of NPOI and other high resolution interferometers is the determination of fundamental stellar parameters in binary systems. In this paper, we elaborate on the procedures used to reduce and analyze NPOI data, including new observations of two spectroscopic binaries selected from the catalog by Batten *et al.* (1989), Mizar A (ζ^1 Ursae Majoris, HR 5054, $V = 2.27$ mag) and Matar (η Pegasi, HR 8650, $V = 2.94$ mag). Both stars had been observed previously with the Mark III optical interferometer by Hummel *et al.* (1995; hereafter H95) and Hummel & Armstrong (1992), who also first determined their visual orbits. Because the orbit of Matar was preliminary, and some new data have since been collected with NPOI, we combined the data of the two interferometers for verification and better phase coverage. In order to determine the component masses in Matar, we combined the interferometry with spectroscopy of the primary of this single-lined spectroscopic binary and with the trigonometric parallax measured by Hipparcos (ESA 1997). In the case of Mizar A, sufficient data had been collected so that a new orbit was computed from the NPOI data alone and combined with published radial velocity data for both components in order to obtain directly the masses and dimensions in this double star system. The new results change slightly the previously published elements for Mizar A and also improve their accuracy. We did not opt for a combination of Mark III and NPOI data in order to derive an independent set of orbital elements.

In the following sections, titled accordingly, we describe the NPOI observations, data reduction, and calibration of the visibilities, which are the primary observables of an interferometer. We then derive relative positions of the binary components and other component parameters from modeling the measured visibilities and derive subsequently the orbital elements and masses from fitting to the relative positions and radial velocities from spectroscopy, as described in the section preceding the discussion. We also obtain a map of Matar from the calibrated visibilities. In the discussion section, we finally derive physical parameters of the stars and compare the results to other investigations.

2. Mark III interferometry

Procedures for observations with the Mark III interferometer on Mt. Wilson, California, as well as for data reduction, calibration, and modeling were described by H95. Observations with the Mark III were done one baseline at a time, with the longest available one being 31.5 m. The squared visibility amplitude, V^2 , was measured at $\lambda\lambda$ 450 nm, 500 nm, 550 nm, and at 800 nm. The Mark III observation dates of Matar, as well as the number of visibility measures obtained are listed in Table 2.

3. NPOI Observations

The NPOI was configured as described by Benson *et al.* (1997). We combined the light detected by the center (C), east (E), and west (W) siderostats of the astrometric subarray which form baselines with lengths of 18.9 m (CE), 22.2 m (CW), and 37.5 m (EW). The pupil plane beam combiner reserves a separate output for each baseline, which is dispersed by a prism and then focused by a lenslet array onto 32 avalanche photo diodes (APDs). The total bandwidth spans 450 nm to 850 nm. The interference fringes are detected on

each baseline by observing the intensity variations created by modulating the path length difference. Vacuum optical delay lines, controlled by laser interferometers, are used to track changes in the position of the fringe pattern due to Earth rotation and atmospheric turbulence. The change in fringe phase with wave number determined from the dispersed fringe pattern is used to derive an error signal in order to keep the fringe packet centered at zero residual delay (“group delay fringe tracking”).

An individual observation, or scan, lasts typically for 90 s. Data, including the photon count rate of every channel in eight temporal bins adjusted synchronous with the modulating delay line stroke, as well as delay line positions and narrow angle tracker quad cell count rates are recorded every 2 ms, but only when the array is tracking fringes on all three baselines.

Program star and calibrator (i.e., a weakly resolved or unresolved single star) scans are interleaved, with 100 being a typical number obtained in a clear night under good seeing conditions. (The seeing statistics at the NPOI site were documented by Hutter *et al.* 1997.) After each scan, a background measurement is taken on blank sky near the star. (The photometric field of view for NPOI is about 2.5 arcseconds.) For calibrators, we generally used γ UMa (HR 4554) and η UMa (HR 5191) for Mizar A, and π^2 Peg (HR 8454) and γ Peg (HR 39, an unresolved spectroscopic binary) for Matar. Their angular diameters are estimated to be less than one milliarcsecond (mas), using a calibration obtained by Mozurkewich *et al.* (1991) based on the apparent visual magnitude, V , and the $(R - I)$ color index of the stars. The NPOI observation dates of Mizar A and Matar, as well as the number of visibility measures obtained are listed in Tables 1 and 3, respectively.

4. NPOI data reduction

Here we describe first which fringe parameters are computed from the data, and then how the data are processed and averaged.

4.1. Visibility amplitudes and phases

To determine the complex fringe visibility, \mathbf{V} , we compute the Fourier transform of the bin counts as a function of time. Let the bin counts be B_j , $j = 0, \dots, 7$; then the real, X , and imaginary part, Y , of $\mathbf{V} = X + iY$ are given by

$$X = \Re(\mathbf{V}) = \sum_{j=0}^{n-1} B_j \cos\left(\frac{2\pi jk}{n}\right) \Bigg|_{k=1} = (B_0 - B_4) + (B_1 - B_3 - B_5 + B_7)/\sqrt{2}, \quad (1)$$

$$Y = \Im(\mathbf{V}) = \sum_{j=0}^{n-1} B_j \sin\left(\frac{2\pi jk}{n}\right) \Bigg|_{k=1} = (B_2 - B_6) + (B_1 + B_3 - B_5 - B_7)/\sqrt{2}. \quad (2)$$

Here, $n = 8$, the number of bins, and $k = 1$, to select the component corresponding to the modulation frequency of one fringe per stroke of n bins.

X and Y have expectation values proportional to $|\mathbf{V}| \sin \phi$ and $|\mathbf{V}| \cos \phi$, respectively, where $|\mathbf{V}|$ and ϕ are the fringe amplitude and phase. ($\mathbf{V} = X + iY = |\mathbf{V}|e^{i\phi}$.) These parameters cannot be averaged for more than a few ms because the variations of ϕ due to the atmosphere will force the mean values toward zero (unless a fringe tracking algorithm is used to determine and correct for the phase variations). Consequently, we chose to incoherently average (a function of) the fringe amplitude.

The unbiased estimator for the square of the visibility amplitude is given by

$$V^2 = 4 \left[\frac{\pi/n}{\sin(\pi/n)} \right]^2 \frac{\langle X^2 + Y^2 - Z^2 \rangle}{\langle N - D \rangle^2}, \quad (3)$$

where $N = \sum_{j=0}^{n-1} B_j$ is the total photon count rate in 2 ms, and D is the background rate. The correction for autocorrelation noise in the numerator, Z^2 , is equal to N in the case of

Poisson statistics. Since some of our detectors exhibit non-Poisson noise (possibly due to after-pulsing of the APDs), we estimate the bias by calculating with Eq. 2 the power at a higher frequency ($k = 4$), giving $Z = B_1 - B_2 + B_3 - B_4 + B_5 - B_6 + B_7 - B_8$. This procedure led to a much smoother variation of the squared visibility amplitude with channel.

We note that it is necessary to integrate V^2 instead of \mathbf{V} (which is used in radio and infrared heterodyne interferometry) because of the incoherent integration forced on us by Earth’s turbulent atmosphere. Recovering the visibility amplitude $|\mathbf{V}|$ by simply taking a square root after averaging the data results in asymmetric error bars except in situations of high signal-to-noise ratios. By taking the square root before averaging the data one can produce an estimator for $|\mathbf{V}|$, but in that estimator the noise bias depends on the mean value of the visibility – not the mean value of the estimate – so that correcting for the bias is not straightforward.

Hajian *et al.* (1998) computed the complex product of the visibility on all three NPOI baselines (the “triple product”) for another unbiased fringe parameter estimator. The phase part of the triple product, ϕ_{123} , is also known in radio interferometry as the closure phase and plays a crucial role in allowing the visibility phases to be recovered in a hybrid self-calibration process (which uses image, i.e., model phases to substitute missing phase information in the closure phases) so that images can be made by inverse Fourier transforming the visibility data. The complex triple product can be averaged for times long compared to the atmospheric coherence time since its phase is not corrupted by atmospheric refractive index fluctuations. The amplitude of the complex triple product is just $V_1 V_2 V_3$, where $V_i = |\mathbf{V}_i|$ is the visibility amplitude on baseline i . No bias correction is required for the triple product, since the noise from the three detector arrays receiving the signal from each baseline is uncorrelated.

4.2. Processing of the data

The raw data sampled at 500 Hz are averaged into segments of 1 s, called data points. Uncertainties were derived from the variance of the 2 ms samples, divided by $\sqrt{500}$. Individual locks, defined as intervals of uninterrupted fringe tracking, can be identified at this stage but are currently ignored. The squared visibility amplitude is averaged, while the complex triple product is vector averaged over the length of each data point (i.e., real and imaginary parts are averaged separately).

The narrow angle tracker quad cell count rates are used to compute image offsets; their variance is also calculated for each point. The delay line positions are referenced to one of the delay lines, and averaged using quadratic polynomial fits to account for curvature due to changes in the geometric delay during the integration interval.

The data are now being edited, further averaged over a scan, and calibrated using interactive software and displays. Editing depends on the variance of the laser metrology and the narrow angle tracker signals to indicate bad data. Dropouts and outliers are also removed in the photon count rate and visibility data using a median filter. The fraction of edited data is typically less than a few percent. However, due to photon count rates of less than about 10 per 2 ms and the poor resulting signal-to-noise ratio, the data from the channels blueward of 520 nm must be discarded.

Incoherent and vector scan averages were performed in a similar manner. The error bars are set equal to the standard deviation of the 1 s data points, divided by the square root of the number of points in a scan. This procedure was chosen instead of propagating the errors from the 1 s data points, because their fluctuations (in case of V^2) were about four times the expected level, indicating the presence of non-white noise sources related to either atmospheric or instrumental effects.

5. NPOI Calibration

Accurate calibration procedures for optical interferometry data were developed by Mozurkewich *et al.* (1991) with the Mark III interferometer. Realizing that atmospheric turbulence has the largest degrading effect on V^2 , they utilized the correlation, closely followed by all calibrators regardless of their position in the sky, between V^2 and the jitter (variance) of the measured baseline delay. Normalization factors for the squared visibility amplitudes of the program stars were then derived from their associated delay jitter. With the NPOI, we use the jitter of the baseline delay as a measure of temporal seeing (i.e. the coherence time), and the variance of the narrow angle tracker offsets as a measure of spatial seeing (i.e. the coherence length). The temporal and spatial coherences are to some extent correlated via the wind speed (Taylor’s frozen turbulence hypothesis, see, e.g. Buscher *et al.* 1995). This is evident in Fig. 1, which shows that delay jitter increases with increasing track jitter, but the correlations are not usually this pronounced.

In general, the usefulness of the tracking jitter has been limited, so that we only considered correlations of V^2 with time or delay jitter. The seeing conditions can change significantly on time scales of an hour, as shown in Fig. 2. On the same night and baseline (CE), V^2 of the calibrators varied systematically (Fig. 3), showing a clear correlation between V^2 and the delay jitter (Fig. 4). In cases where this correlation (using all calibrators) was weak, we smoothed systematic variations of V^2 with time in the calibrator closest to the program star with low-order polynomials or a Gaussian function. By doing this, we minimize visibility degradation which depends on the position in the sky, and which does not correlate well over large angles. Each channel was calibrated separately using a combination of these procedures.

Variations of the calibrator squared visibilities and triple amplitudes from scan to scan were typically larger than the statistical uncertainties. In order to arrive at a more

realistic uncertainty of the calibrated visibilities, we increased the uncertainties by adding a calibration uncertainty in quadrature to the statistical uncertainty of the amplitudes. The calibration uncertainty was determined such that the reduced χ^2 , χ^2_ν , of a fit of a constant to the calibrator visibility amplitudes would be unity. Typical calibration uncertainties ranged from 5% to 15% for the squared visibility amplitudes, and from 10% to 20% for the triple amplitudes.

Deviations of the closure phase of the calibrators from zero were smoothed as a function of time using low order polynomials or Gaussian functions. Each channel was calibrated independently from the other channels. Figure 5 shows the closure phases of the calibrators as a function of time. The variations are caused by thermal drifts in the alignment of the beam combiner optics, related to variations of the temperature or settling of it after visits of the observer to the beam combiner room. The closure phase variations amounted to typically less than about 10 degrees per hour averaged over the entire night. Phase calibration uncertainties were typically only one to four degrees, as there are fewer instrumental systematic influences. But again, a calibration uncertainty was derived from the residual variations of the calibrated phase and added in quadrature to the statistical uncertainties.

6. Modeling

The aim of this investigation is the determination of stellar parameters (e.g., diameters, luminosities, masses) and orbital elements (angular semimajor axis a , eccentricity e , period P , epoch of periastron passage T , inclination i , position angle of the ascending node Ω , and the argument of the periastron ω) of two double stars, Mizar A and Matar. These stars are detached, non-variable, and non-interacting systems, so that a small set of parameters is sufficient to describe the observations. We combined interferometric, spectroscopic, and

astrometric data in order to solve directly for these parameters. This method effectively reduces the total number of solution parameters (unknowns) required over the case where each data set is modeled separately. We have verified the mutual consistency of the data by separate modeling or checking the published elements of the spectroscopic orbits before the data were combined. Data weights were adopted such that separate fits would yield $\chi^2_\nu \approx 1$. We used the Levenberg-Marquardt algorithm for non-linear least squares fits, as implemented by Press *et al.* (1992). All derivatives with respect to parameter variations were computed numerically.

6.1. Mizar A

Images of Mizar A, No. 764 in the catalog by Batten *et al.* (1989) (FK 497, HR 5054, HD 116656, HIC 65378) were made by Benson *et al.* (1997) from NPOI data, and show two unresolved and detached components. The spectral classification of each component is the same and equal to A2V, according to Hoffleit & Jaschek (1982). For such a simple structure, we chose to model the visibility data of each night with relative separation, ρ , and position angle, θ , of two stellar disks, for which we adopted a diameter of 0.8 mas from photometry (H95). (Our baselines are not long enough to determine the component diameters of Mizar A reliably.) Orbital motion (which is significant during a night and has to be corrected for in the single night fit) and a magnitude difference of zero between the components were adopted from a fit of these parameters directly to the combined visibility data of all 25 nights. The adoption of identical components comes from the visibility closure phase jump amplitude of approximately 180 degrees. If a fit is performed to the squared visibility data alone, a wavelength-independent magnitude difference of about 0.2 mag is found, corresponding to a minimum V^2 of 0.05, possibly caused by the bias correction not being complete. The reason that the closure phases dominate the solution for

small magnitude differences is their high sensitivity to changes in the component’s relative brightness, whereas the derivative of the squared visibility amplitude with respect to the magnitude difference approaches zero for identical components.

For each night, we estimated the uncertainty in the relative position measurement by computing the synthesized beam width and dividing by 40; this scaling factor would yield $\chi^2_\nu \approx 1$ for the fit of the orbit to the relative positions. Benson *et al.* (1997) assumed a more conservative scaling factor of 5 which did not account for the data weights and the internal consistency of the position measurements found in this work. However, the wavelength scale has only been measured for one of the three NPOI spectrometers (baselines) by Fourier transform spectroscopy and confirmed to be within 1% of the nominal scale (Hajian *et al.* 1998, in prep.). The scale of the other two spectrometers is currently not better known than to a fraction of the width of the channel which receives the laser metrology light; we adopt a scale error (systematic error) of also 1%. We list the results in Table 1; columns 1 and 2 give date and fractional Julian year of the observation (at 7 UT), column 3 the number of measured visibilities, columns 4 and 5 the derived separation and position angle (equinox = mean epoch at local midnight on the date of the observation), columns 6 to 8 the axes and the position angle of the uncertainty ellipse, and column 9 the deviation of the fitted relative binary position (ρ, θ) from the model values. Position angles are measured counterclockwise from north. (The Besselian year, By , used in previous publications, can be computed from the Julian year, Jy , as $By = 1.00002136 \times Jy - 0.0414$.)

In Figs. 6, 7, and 8 we give examples of the fit to the visibility data from May 15, 1997. Each plot corresponds to an individual scan, for which the visibility data are plotted versus the wavelength of the channels. Small systematic variations due to imperfect calibrations can be seen from scan to scan, while the data show smaller variations from channel to channel.

Orbital elements fitted to the visibilities directly and to the set of relative positions agree very well. Those in common with elements of the spectroscopic orbit are in good agreement with results obtained by Fehrenbach & Prevot (1961). In order to improve the precision of the period determination and to include the masses as fit variables, we combined radial velocity data and position data. The resulting set of our final orbital elements and component parameters is listed in Table 4. The orbit is shown in Fig. 11; the fits to the radial velocity data are shown in Figs. 9 and 10 for each component. The average deviation of the derived positions from the orbit is less than 100 microarcseconds. Comparison with the results given in H95 yields reasonable agreement (within about 3σ). Parameter uncertainties might have been somewhat underestimated by H95 for this particular star because of a companion 14 arcseconds away but within the photometric field of view, which required solving for additional calibration constants. This companion is not within the field of view for NPOI, so that the light of the secondary does not affect the measured visibility.

6.2. Matar

The spectrum of Matar, No. 1396 in the catalog by Batten *et al.* (1989) (FK 857, HR 8650, HD 215182, HIC 112158) is a composite of spectral types G2II-III and F0V, according to Hoffleit & Jaschek (1982). Even though only the velocity of the giant primary component has been measured (Crawford 1901, Parsons 1983), we can obtain the component masses by adding a measurement of the trigonometric parallax by Hipparcos to the data from interferometry and spectroscopy. A preliminary visual orbit of Matar had been derived first from observations with the Mark III interferometer (Hummel & Armstrong 1992), and the new NPOI observations were used to improve the phase coverage.

We started by fitting component parameters (and orbital elements) directly to the visibility data. The secondary is unresolved and estimated to be 0.3mas in diameter.

The primary component of Matar is significantly resolved on the longer baselines used by the Mark III and NPOI, so that its diameter could be determined directly from the fit. We adopted linear limb darkening coefficients appropriate for a luminosity class III star with an effective temperature of 5000 K, using tables published by Van Hamme (1993). The coefficients are 0.834 at 450 nm, 0.713 at 550 nm, and 0.514 at 800 nm; values at intermediate wavelengths were interpolated. The limb darkened diameter is about 5% (10%) larger than the uniform disk diameter at 800 nm (450 nm). The resulting diameter (3.06 mas) is in very good agreement with the limb darkened diameter (3.045 mas) determined by Blackwell *et al.* (1991) using the Infrared Flux Method. Even though Blackwell *et al.* have not accounted for the flux of the secondary, its influence is minimal because it contributes no significant infrared flux compared to the cooler primary, and it is much less luminous (by a factor of 10, see Table 6). The magnitude differences of the components in the green, yellow, and red (using a quadratic polynomial to interpolate values in between) complete the set of component parameters fit to the visibility data.

The set of relative positions was then obtained adopting the component parameters from the previous step, and is listed in Table 2 (Mark III) and Table 3 (NPOI). For the final fit of masses and orbital elements to the combination of relative positions, radial velocities, and the trigonometric parallax, a value for the latter had to be adopted between the values of 15.18 ± 0.56 mas given in the Hipparcos catalog and 16.48 ± 0.98 mas given by Martin & Mignard (1998). Even though these determinations, which accounted for orbital motion of the binary, are consistent with each other, they would yield masses differing by 18% of their mean. We chose the Hipparcos catalog value since it has the smaller uncertainty. A larger parallax would result in smaller masses and luminosities. The results of the fit are listed in Table 4. The orbit is shown in Fig. 12, and the fit to the radial velocity data is shown in Fig. 13. A detailed magnification showing some of the NPOI relative positions is shown in Fig. 14, along with the prediction using the elements published by Hummel & Armstrong

(1992). Even though the 1992 elements were based on a limited data set, the agreement with the new NPOI measurements is quite good.

In Figs. 15, 16, and 17 we give examples of the fit to the visibility data on October 17, 1997. Small systematic variations can be seen from scan to scan, while the data shows smaller variations from channel to channel. We used this night’s data to make an image of Matar, which is shown in Fig. 18. The procedures used were the same as described by Benson *et al.* (1997).

Although the Hipparcos observations did not have enough resolution to separate the two components in Matar, they provided the periodic motion of the photo center due to orbital motion. We list the elements of the photo center orbit in Table 4; there is clearly good agreement with the orbital solution of this work. With the sizes of the semi-major axes, a_1 and a_2 , of the two component orbits with respect to the system center of mass from our orbital analysis, we can predict the photo center semi-major axis, a_{PC} , using the relative flux of the components across the Hipparcos detector band interpolated between the derived magnitude differences (in the green, yellow, and red), and the actual Hipparcos detector response function (as published in the catalog). The magnitude difference in the Hipparcos system is $\Delta H_p = 2.60$ mag, corresponding to a flux ratio of $f_1/f_2 = 11$. With $a_1 = 172 \times 10^6$ km and $a_2 = 271 \times 10^6$ km, $a_{PC} = (a_1 f_1 - a_2 f_2)/(f_1 + f_2) = 13.7$ mas, in very good agreement with the measurement by Hipparcos. It is interesting to compare these results to measurements of parallax (10 ± 7 mas) and photocenter semi-major axis (22 ± 6 mas) done several decades ago by Van de Kamp & Damkoehler (1957) using the 24-inch Sproul refractor and photographic plates.

7. Discussion

7.1. Mizar A

We derive an orbital parallax of $\pi_{\text{orb}} = 39.4 \pm 0.3$ mas, somewhat larger than the value published by H95 ($\pi_{\text{orb}} = 38.3 \pm 0.4$ mas). However, we find a significant difference between our orbital parallax and the trigonometric parallax from Hipparcos ($\pi_{\text{trig}} = 41.7 \pm 0.6$ mas). Systematic errors in any of the involved data sets could be responsible. We think this is less likely for the NPOI data because its map scale agrees to within a fraction of a percent with the Mark III scale as demonstrated by the Matar measurements (see Fig. 15). On the other hand, the comparison of the components' velocity amplitudes measured by Fehrenbach & Prevot (1961) with earlier determinations listed by Cesco (1946) indicates that the available spectroscopy (and not the Hipparcos parallax) might be the limiting factor. A systematic Hipparcos parallax error is not ruled out either since Mizar A ($V = 2.27$ mag) is the brighter component of A.D.S. 8891 and the companion (B, ζ^2), which is $V = 3.95$ mag at about $14''$, is a spectroscopic binary too with an orbital period of 175 days. Depending on the semi-major axis and the magnitude difference between the components of Mizar B, a noticeable distortion of the point-spread-function might have introduced an error in the Hipparcos solution which assumed only the presence of two single components A and B (C. Martin, priv. comm.).

In Table 5 we list the derived physical parameters for Mizar A based on the assumption of identical components. Combined apparent magnitudes are adopted from Johnson *et al.* (1966) and are $B = 2.29$, $V = 2.27$, and $I = 2.33$. We estimated an uncertainty in the magnitude differences of 0.02 mag and adopted an effective temperature corresponding to an A2 dwarf (Flower 1977, 1996) with an uncertainty of one subtype, corresponding to the uncertainty in the individual colors. Using formulas provided by Gubochkin & Miroshnichenko (1991), we derive a value for the bolometric correction from the effective

temperature. Thus, we obtain the bolometric luminosities and predicted stellar radii. The predicted angular diameters are 0.87 ± 0.04 , consistent with the value adopted from photometry. The results do not differ significantly from those obtained by H95. Derived quantities K_1 and K_2 agree well with the values ($K_1 = 68.80 \pm 0.79$ km/s, $K_2 = 67.60 \pm 0.91$ km/s) determined by Fehrenbach & Prevot (1961).

7.2. Matar

In order to derive the physical parameters for Matar as listed in Table 6, we adopted for the primary the effective temperature and its uncertainty as determined by Blackwell *et al.* (1991), and for the secondary a temperature derived from its $(B - V)$ color index using tables by Flower (1996). (The uncertainty in the secondary’s temperature corresponds to its uncertainty in color.) The tables by Flower (1996) also show that Matar’s primary is slightly redder (by 0.06 mag) than what one would expect from the temperature, and the spectral type of the primary should be more like G5 (Flower 1977). A supergiant of type G2 would have the right color and temperature, its predicted diameter (Schmidt-Kaler 1982), however, would be much larger than the one we derived. (ϵ Geminorum, a G8 supergiant, has an angular diameter of 4.8 mas as derived by the Mark III Interferometer [Mozurkewich, in prep.] and NPOI [Pauls, in prep.], which translates into a linear radius of about 140 solar radii using the trigonometric parallax measured by Hipparcos, $\pi_{\text{trig}} = 3.6$ mas.) Combined apparent magnitudes of Matar were adopted as $B = 3.81$, $V = 2.95$, and $I = 2.08$. The predicted angular diameter of the primary of Matar is 3.0 ± 0.2 mas (21 solar radii), consistent with the fitted limb darkened diameter.

The mass determination for the components of Matar is not very precise due to the uncertainty in the parallax. Based on color, luminosity and mass, the secondary is likely to be an A5 dwarf. The primary of Matar is definitively more luminous and larger than a

giant of its type (Schmidt-Kaler 1982), putting it into the bright giant class.

8. Conclusions

We have analysed interferometric observations of two double stars, obtained with the NPOI and Mark III interferometers. With only a few scans each of which contains 90 s data, the new three-station NPOI is able to measure the relative positions of the components with a precision typically better than 0.1 mas. This work represents the current state of the art at one of the major optical interferometer arrays currently in operation. As the development of this new type of instrument parallels the early history of Very Long Baseline Interferometry in the radio, we can expect a fundamental impact of this very high resolution technique on stellar astrophysical research in the years to come.

We thank the observers D. Black, B. Burress, and C.S. Denison for their careful operation of the NPOI array under the supervision of Dr. J. A. Benson, and H.-H. Nguyen for help with the data reduction. This work was funded by the Office of Naval Research and the Oceanographer of the Navy. This research has made use of the SIMBAD literature database, operated at CDS, Strasbourg, France.

REFERENCES

- Armstrong, J. T., Hutter, D. J., Johnston, K. J., & Mozurkewich, D. 1995, *Physics Today*, 48/5, 42
- Armstrong, J. T., Mozurkewich, D., Rickard, L. J., Hutter, D. J., Benson, J. A., Bowers, P. F., Elias II, N. M., Hummel, C. A., Johnston, K. J., Buscher, D. F., Clark III, J. H., Ha, L., Ling, L.-C., White, N. M., & Simon, R. S. 1998, *ApJ*, 496, 550
- Batten, A. H., Fletcher, J. M., & MacCarthy, D. G. 1989, *Pub. Dom. Astrophys. Obs.*, 17, 1
- Benson, J. A., Hutter, D. J., Elias II, N. M., Bowers, P. F., Johnston, K. J., Hajian, A. R., Armstrong, J. T., Mozurkewich, D., Pauls, T. A., Rickard, L. J., Hummel, C. A., White, N. M., Black, D., & Denison, C. S. 1997, *AJ*, 114, 1221
- Blackwell, D. E., Lynas-Gray, A. E., & Petford, A. D. 1991, *A&A*, 245, 567
- Buscher, D. F., Armstrong, J. T., Hummel, C. A., Quirrenbach, A., Mozurkewich, D., Johnston, K. J., Denison, C. S., Colavita, M. M., & Shao, M. 1995, *Applied Optics*, 34, 1081
- Cesco, C. U. 1946, *ApJ*, 104, 287
- Crawford, R. T. 1901, *Lick O. Bull.*, 1, 27
- ESA 1997, *The Hipparcos and Tycho Catalogues*, European Space Agency SP-1200
- Fehrenbach, Ch., & Prevot, L. 1961, *J.Obs.*, 44, 83
- Flower, P. J. 1977, *A&A*, 54, 31
- Flower, P. J. 1996, *ApJ*, 469, 355
- Gubochkin, A. N., & Miroshnichenko, A. S. 1991, *Kin. and Phys. of Cel. Bodies*, 7, 59

- Hajian, A. R., Armstrong, J. T., Hummel, C. A., Benson, J. A., Mozurkewich, D., Pauls, T. A., Hutter, D. J., Elias II, N. M., Johnston, K. J., Rickard, L. J., & White, N. M. 1998, *ApJ*, 496, 484
- Hoffleit, D., & Jaschek, C. 1982, *The Bright Star Catalogue* (Yale University Observatory, New Haven)
- Hummel, C. A., & Armstrong, J. T. 1992, in: *Complementary Approaches to Double and Multiple Star Research*, ed. by H. A. McAlister and W. I. Hartkopf (San Francisco: PASP), p. 552
- Hummel, C. A., Armstrong, J. T., Buscher, D. F., Mozurkewich, D., Quirrenbach, A., & Vivekanand, M. 1995, *AJ*, 110, 376 (H95)
- Hutter, D. J., Elias II, N. M., Peterson, E. R., Weaver, W. B., Weaver, G., Mozurkewich, D., Vrba, F. J., Buscher, D. F., & Hummel, C. A. 1997, *AJ*, 114, 2822
- Johnson, H. L., Mitchell, R. I., Iriarte, B., & Wiśniewski, W. Z. 1966, *Comm. Lunar Planetary Lab.*, 4, 99
- Martin, C., & Mignard, F. 1998, *A&A*, 330, 585
- Mozurkewich, D., Johnston, K. J., Simon, R. S., Bowers, P. F., Gaume, R. A., Hutter, D. J., Colavita, M. M., Shao, M., & Pan, X. P. 1991, *AJ*, 101, 2207
- Parsons, S. B. 1983, *ApJS*, 53, 553
- Press, W. H., Flannery, B. P., Teukolsky, S. A., & Vetterling, W. T. 1992, *Numerical Recipes* (Cambridge University Press, Cambridge)
- Schmidt-Kaler, T. H. 1982, *Physical Parameters of the Stars*, in: *Landolt-Bornstein New Series*, Vol. 2b, ed. by K. Schaifers and H. H. Voigt (Springer Verlag, New York)
- Van Hamme, W. 1993, *AJ*, 106, 2096

Van de Kamp, P., Damkoehler, J. E. 1957, AJ, 62, 393

Table 1: NPOI observation and result log for Mizar A

	Julian	No.	ρ	θ	σ_{maj}	σ_{min}	φ	O-C
UT Date	Year	vis.	[mas]	[deg]	[mas]	[mas]	[deg]	[mas]
(1)	(2)	(3)	(4)	(5)	(6)	(7)	(8)	(9)
May 01	1996.3307	332	6.31	286.81	0.134	0.042	167.0	0.039
May 02	1996.3334	249	7.37	301.77	0.141	0.040	4.1	0.035
May 03	1996.3362	249	7.57	313.86	0.172	0.040	176.6	0.062
May 04	1996.3389	320	7.44	326.39	0.123	0.040	170.5	0.046
May 08	1996.3499	154	7.23	21.44	0.172	0.040	176.6	0.061
May 21	1996.3855	166	5.13	275.71	0.184	0.040	9.5	0.032
May 29	1996.4074	166	7.50	26.34	0.159	0.040	18.4	0.126
Jun 01	1996.4156	300	9.06	59.13	0.131	0.042	22.6	0.036
Jun 04	1996.4238	406	10.24	80.33	0.144	0.042	24.8	0.141
Mar 08	1997.1822	270	7.46	325.27	0.131	0.040	4.4	0.051
Mar 14	1997.1986	178	8.15	44.26	0.137	0.042	162.9	0.022
Mar 20	1997.2150	531	10.04	90.95	0.101	0.045	174.3	0.012
Mar 21	1997.2178	522	9.30	98.89	0.105	0.045	16.7	0.071
Mar 26	1997.2315	276	6.86	292.96	0.151	0.040	0.0	0.058
May 01	1997.3300	680	9.36	97.73	0.091	0.045	6.3	0.012
May 02	1997.3328	680	7.85	107.19	0.122	0.042	24.4	0.032
May 14	1997.3656	292	7.80	38.10	0.186	0.043	40.6	0.114
May 15	1997.3684	1020	8.39	48.35	0.142	0.043	45.0	0.018
May 23	1997.3903	656	6.82	112.96	0.109	0.043	33.7	0.066
May 28	1997.4039	740	7.57	311.40	0.115	0.043	37.9	0.054
May 30	1997.4094	595	7.30	336.38	0.121	0.043	41.6	0.020
Jun 21	1997.4697	312	7.05	356.38	0.149	0.042	28.3	0.036
Jun 22	1997.4724	375	7.08	10.61	0.131	0.043	32.5	0.025
Jun 27	1997.4861	328	9.50	65.22	0.143	0.043	39.3	0.024
Jul 04	1997.5052	492	3.98	136.15	0.165	0.043	52.4	0.078

Table 2: Mark III observation and result log for Matar

	Julian	No.	ρ	θ	σ_{maj}	σ_{min}	φ	O-C
UT Date	Year	vis.	[mas]	[deg]	[mas]	[mas]	[deg]	[mas]
(1)	(2)	(3)	(4)	(5)	(6)	(7)	(8)	(9)
Jun 09	1989.4369	12	39.82	218.72	1.210	0.100	111.7	0.331
Aug 15	1989.6203	27	24.61	240.27	0.340	0.100	84.7	0.080
Aug 25	1989.6477	26	22.77	246.49	0.560	0.090	75.3	0.477
Sep 03	1989.6724	53	20.69	252.62	0.150	0.050	89.2	0.304
Sep 05	1989.6778	42	20.04	254.22	0.150	0.040	87.9	0.076
Sep 10	1989.6915	27	18.77	257.80	0.380	0.110	95.5	0.422
Sep 13	1989.6997	30	17.92	259.15	0.730	0.200	90.6	0.968
Sep 21	1989.7216	26	17.27	269.30	0.370	0.090	83.9	0.114
Sep 22	1989.7244	30	17.03	270.00	0.610	0.130	85.4	0.278
Nov 03	1989.8394	15	17.55	320.53	0.460	0.100	85.9	0.350
Jul 27	1990.5676	53	18.74	76.01	0.150	0.040	97.9	0.146
Aug 04	1990.5895	42	17.78	83.43	0.370	0.090	92.0	0.316
Sep 12	1990.6963	51	18.72	130.02	1.230	0.400	92.0	1.180
Oct 14	1990.7839	24	23.15	151.71	2.460	0.440	78.5	1.582
Oct 17	1990.7921	54	22.99	160.63	1.480	0.320	85.1	1.494
Oct 25	1990.8140	69	25.35	161.64	0.150	0.030	83.5	0.121
Aug 03	1991.5861	35	45.44	212.53	0.270	0.050	84.0	0.071
Aug 04	1991.5889	54	45.35	213.00	0.380	0.090	85.8	0.323
Aug 28	1991.6546	54	41.25	216.87	0.150	0.040	86.1	0.138
Aug 29	1991.6573	68	41.00	216.96	0.140	0.050	87.4	0.068
Sep 18	1991.7121	39	36.99	221.40	0.280	0.050	89.2	0.127
Oct 01	1991.7476	71	34.74	224.64	0.880	0.210	81.2	0.717
Oct 03	1991.7531	78	33.84	225.53	0.320	0.060	94.1	0.323
Oct 19	1991.7969	30	29.78	229.93	0.550	0.130	74.5	0.271
Nov 01	1991.8325	75	26.52	235.10	0.340	0.060	88.5	0.383
Jul 04	1992.5060	33	36.67	25.86	1.560	0.160	100.5	0.436
Aug 06	1992.5964	48	32.83	35.03	0.310	0.090	102.3	0.184
Aug 21	1992.6375	69	30.42	40.22	0.220	0.060	89.6	0.065

Table 3: NPOI observation and result log for Matar

	Julian	No.	ρ	θ	σ_{maj}	σ_{min}	φ	O-C
UT Date	Year	vis.	[mas]	[deg]	[mas]	[mas]	[deg]	[mas]
(1)	(2)	(3)	(4)	(5)	(6)	(7)	(8)	(9)
Jul 03	1997.5025	350	23.31	156.89	0.162	0.040	172.9	0.160
Jul 11	1997.5244	380	24.74	160.79	0.162	0.040	176.4	0.461
Jul 12	1997.5272	354	24.87	161.14	0.162	0.040	176.4	0.577
Jul 16	1997.5381	246	26.73	163.93	0.164	0.041	169.4	0.464
Jul 18	1997.5436	278	26.81	164.64	0.162	0.040	176.4	0.099
Aug 01	1997.5819	793	30.11	170.21	0.141	0.040	4.1	0.172
Aug 02	1997.5846	550	30.03	170.50	0.176	0.040	13.2	0.135
Oct 02	1997.7517	510	42.74	185.69	0.164	0.040	169.4	0.033
Oct 04	1997.7571	486	42.86	186.00	0.144	0.040	12.1	0.193
Oct 16	1997.7900	1533	44.78	188.19	0.125	0.040	14.0	0.239
Oct 17	1997.7927	1482	45.06	188.30	0.125	0.041	14.0	0.106
Oct 18	1997.7955	1744	45.20	188.44	0.132	0.040	8.7	0.114
Oct 21	1997.8037	1112	45.67	188.83	0.144	0.040	12.1	0.090
Nov 08	1997.8530	518	48.12	191.69	0.123	0.041	9.5	0.144
Nov 18	1997.8803	722	49.26	192.91	0.152	0.040	7.6	0.022
Nov 19	1997.8831	450	49.31	193.07	0.152	0.040	7.6	0.080

Table 4: Orbital elements and component parameters from combined fits

Star	Mizar A	Matar	
Data	NPOI	Mark III, NPOI	Hipparcos
	R.V. _{A,B}	$\pi_{\text{Hipparcos}}$, R.V. _A	
a/mas	9.83 ± 0.03^a	45.02 ± 0.06	
$a_{\text{PC}}/\text{mas}^b$			13.60 ± 0.88
$i/^\circ$	60.5 ± 0.3	68.28 ± 0.05	70.6 ± 3.1
$\Omega/^\circ$ (J2000.0)	106.0 ± 0.4	20.90 ± 0.04	23.6 ± 3.5^c
T (JD−244E4)	7636.07 ± 0.02	7140.3 ± 0.4	7170 ± 9
e	0.5354 ± 0.0025	0.1677 ± 0.0009	0.155 ± 0.016^d
$\omega/^\circ$	104.3 ± 0.3	-5.5 ± 0.1	5.6 ± 5.5^d
P/days	20.53835 ± 0.00005	817.41 ± 0.04	818 ± 2.2^d
$\mathcal{M}_1/\mathcal{M}_\odot$	2.43 ± 0.07	3.2 ± 0.4	
$\mathcal{M}_2/\mathcal{M}_\odot$	2.50 ± 0.07	2.0 ± 0.2	
D_1/mas	0.8^e	3.06 ± 0.03	
D_2/mas	0.8^e	< 1	
$\Delta m_{450\text{nm}}$ [mag] ^f	0 ± 0.02	2.01 ± 0.10	
$\Delta m_{550\text{nm}}$ [mag]	0 ± 0.02	2.76 ± 0.05	
$\Delta m_{800\text{nm}}$ [mag]	0 ± 0.02	3.61 ± 0.05	

^aSystematic error 0.1 mas

^bPhoto center

^cOrbit of secondary

^dAdopted from spectroscopy

^eAdopted from photometry

^f $\Delta m \equiv m_2 - m_1$

Table 5: Derived physical parameters of Mizar A

Parameter	Primary (A2V)	Secondary (A2V)
$K[\text{km/s}]$	69.1	67.2
$D[\text{pc}]$	25.4 ± 0.3	
$(B - V)$	0.02 ± 0.03	
T_{eff}/K	9000 ± 200	
BC	-0.09 ± 0.06	
M_{bol}	0.91 ± 0.07	
L/L_{\odot}	33.3 ± 2.1	
R/R_{\odot}	2.4 ± 0.1	

Note: values listed are for each component separately

Table 6: Derived physical parameters of Matar

Parameter	Primary (G2II-III)	Secondary (A5V)
$K[\text{km/s}]$	14.5	22.8
$D[\text{pc}]$	65.9 ± 2.4	
$(B - V)$	0.94 ± 0.03	0.2 ± 0.1
T_{eff}/K	5100 ± 25	7800 ± 600
BC	-0.27 ± 0.05	0.02 ± 0.05
M_{bol}	-1.32 ± 0.10	1.72 ± 0.11
L/L_{\odot}	262 ± 23	15.8 ± 1.6
R/R_{\odot}	20.9 ± 0.8	2.2 ± 0.2

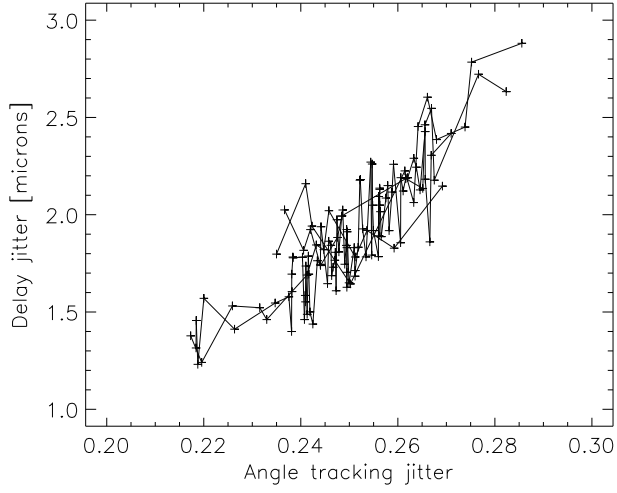


Fig. 1.— Correlation of delay and angle tracking jitter on baseline CE, for 1997-07-25. Only data of calibrators are shown. The track jitter is defined as the r.m.s. variance of the narrow angle tracker error signal in units of the Airy disk diameter.

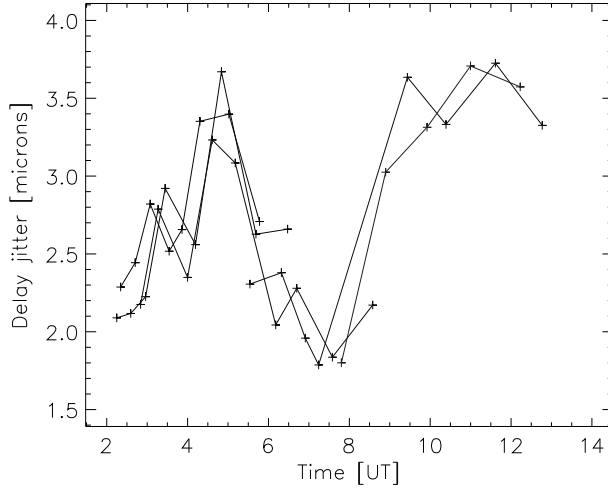


Fig. 2.— Delay jitter on baseline CE as a function of time, for 1997-03-26.

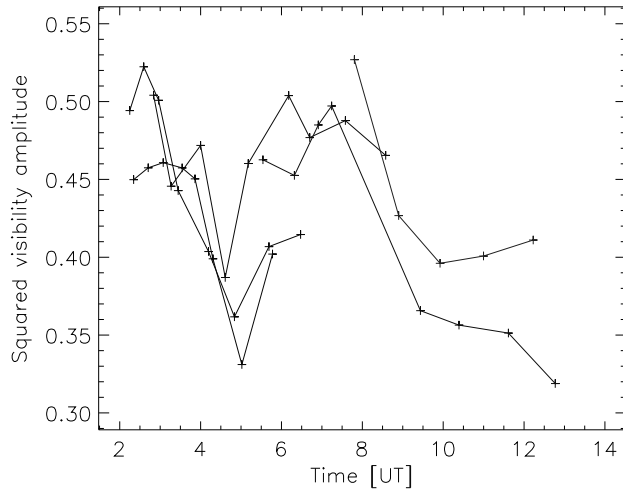


Fig. 3.— Calibrator visibilities (baseline CE, channel 5, 744 nm) as a function of time, for 1997-03-26.

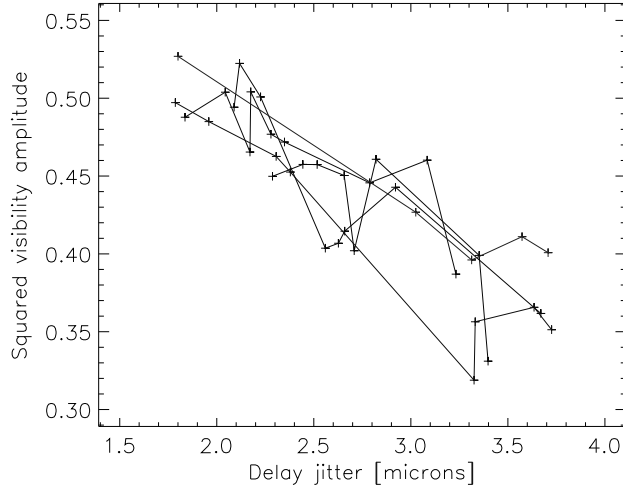


Fig. 4.— Correlation of calibrator visibilities (baseline CE, channel 5, 744 nm) and delay jitter, for 1997-03-26.

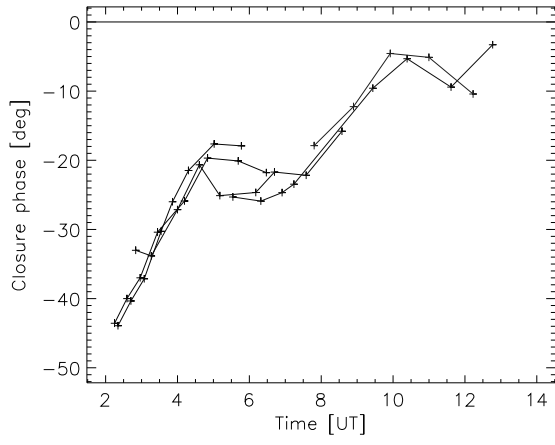


Fig. 5.— Closure phase (channel 5, 744 nm) as a function of time, for 1997-03-26.

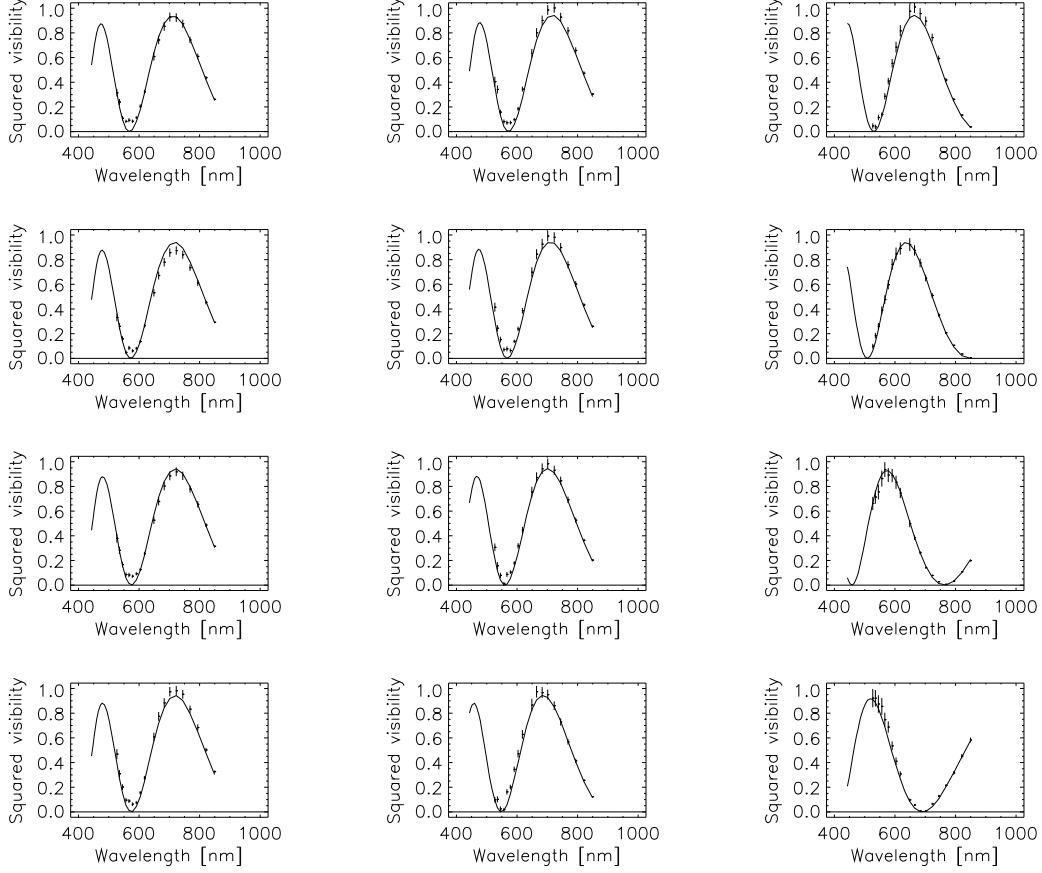


Fig. 6.— Squared visibility amplitudes of Mizar A on the EW baseline versus wavelength for 12 scans obtained during May 15, 1997, between 7 UT and 10.5 UT. Solid lines are model values based on parameters in Table 4. Note that the smallest visibilities usually show a positive bias.

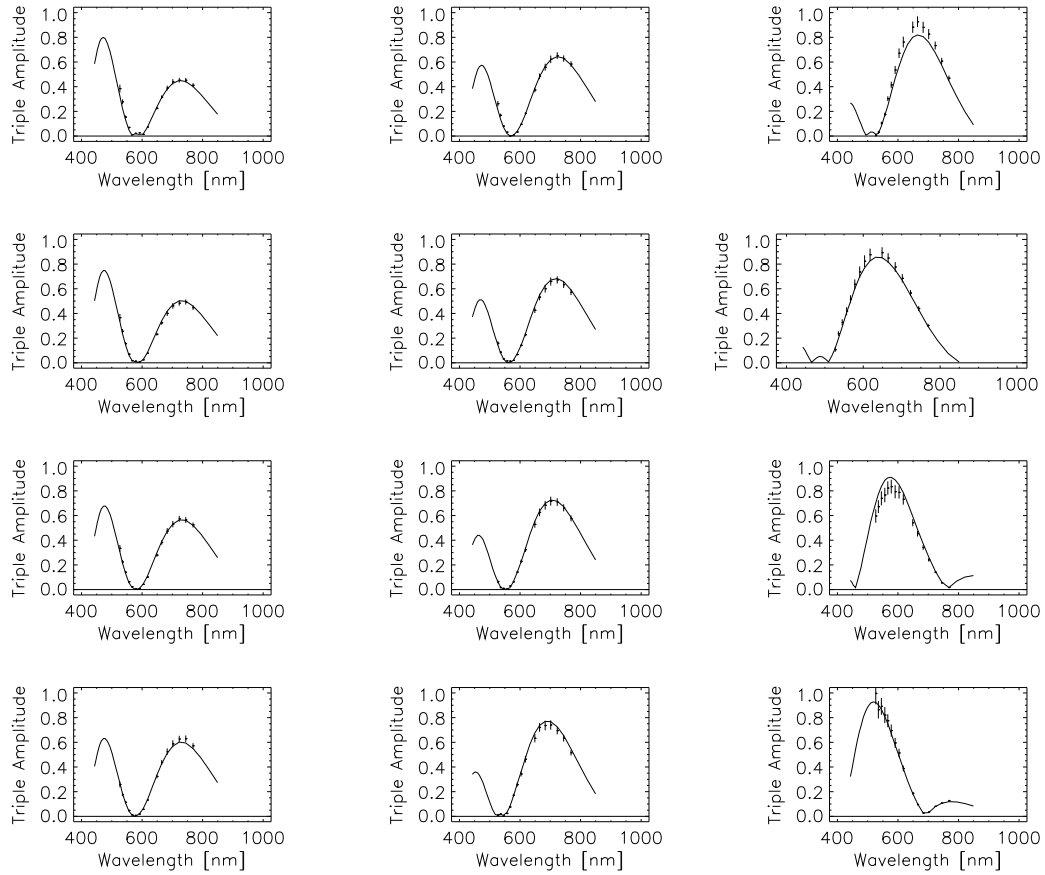


Fig. 7.— Triple amplitudes of Mizar A versus wavelength for 12 scans obtained during May 15, 1997. Solid lines are model values based on parameters in Table 4.

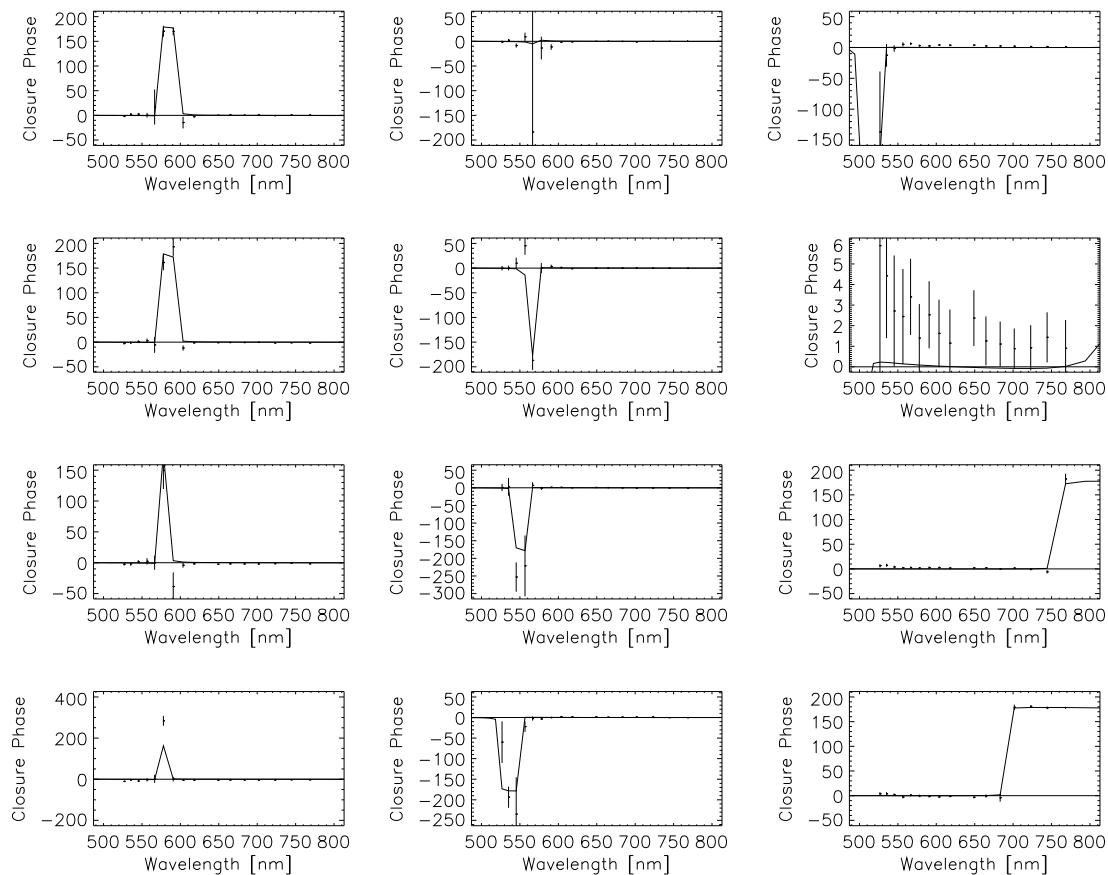


Fig. 8.— Closure phases (in degrees) of Mizar A versus wavelength for 12 scans obtained during May 15, 1997. Solid lines are model values based on parameters in Table 4.

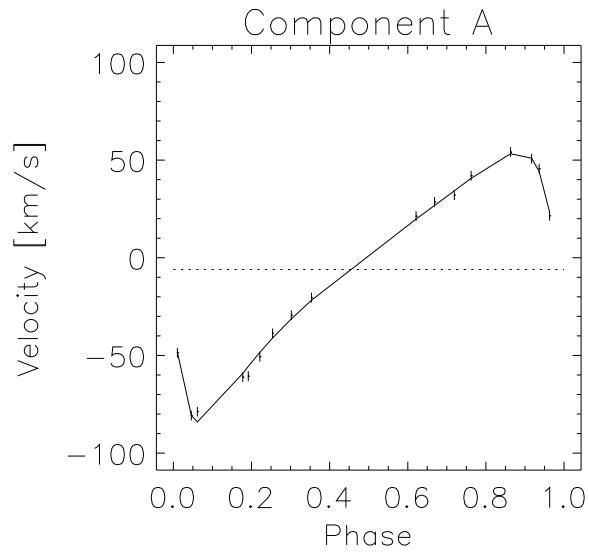


Fig. 9.— Spectroscopic orbit of the primary of Mizar A.

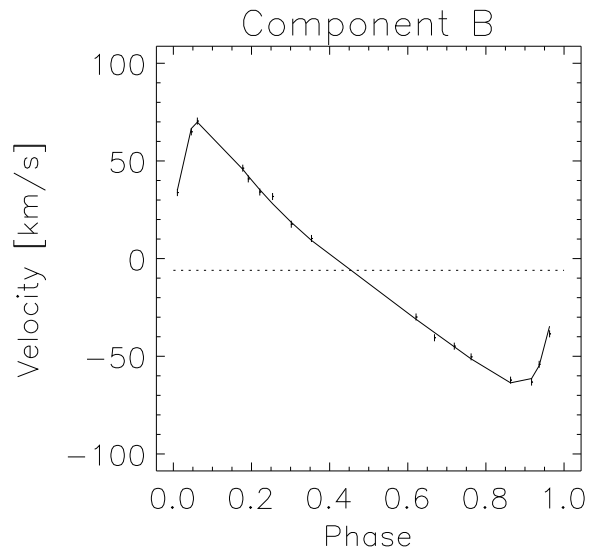


Fig. 10.— Spectroscopic orbit of the secondary of Mizar A.

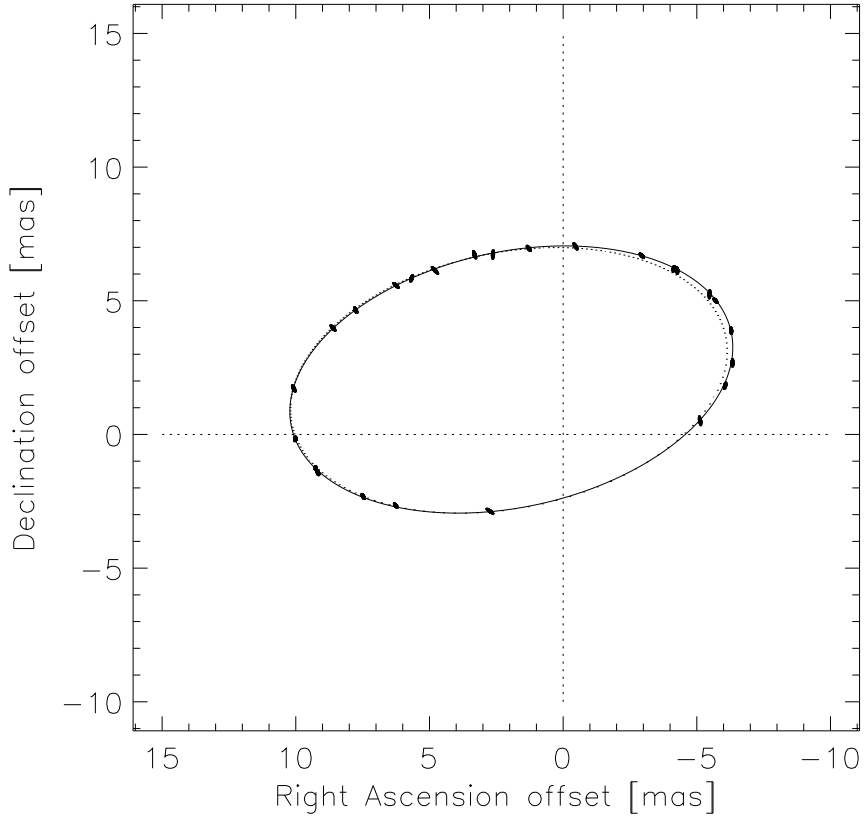


Fig. 11.— Apparent interferometric orbit of Mizar A with NPOI measurements. The dotted line is the orbit published by H95 based on Mark III observations, which did not cover the north-west quadrant.

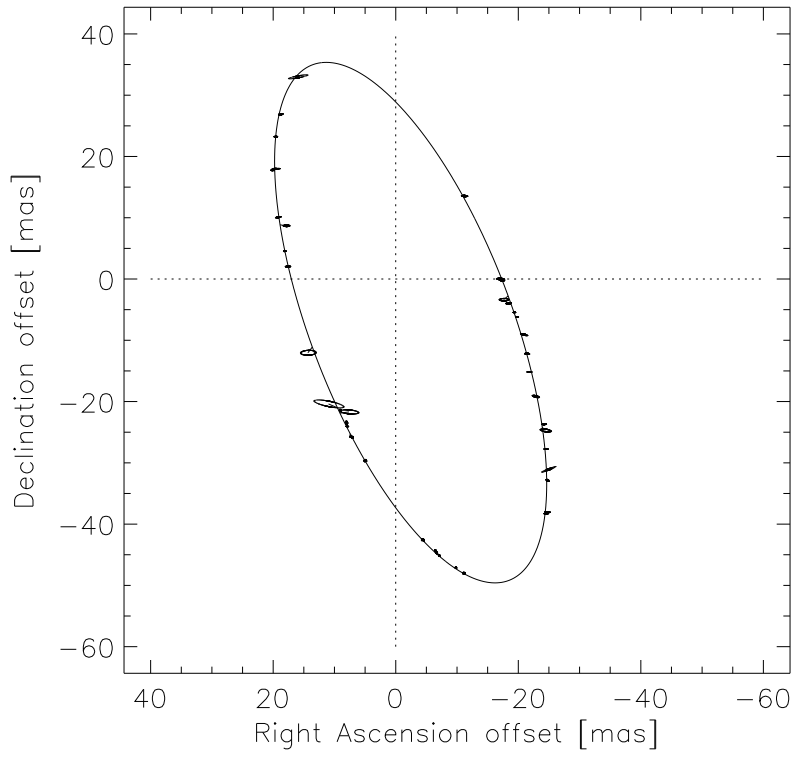


Fig. 12.— Apparent interferometric orbit of Matar, including data from the Mark III interferometer and NPOI.

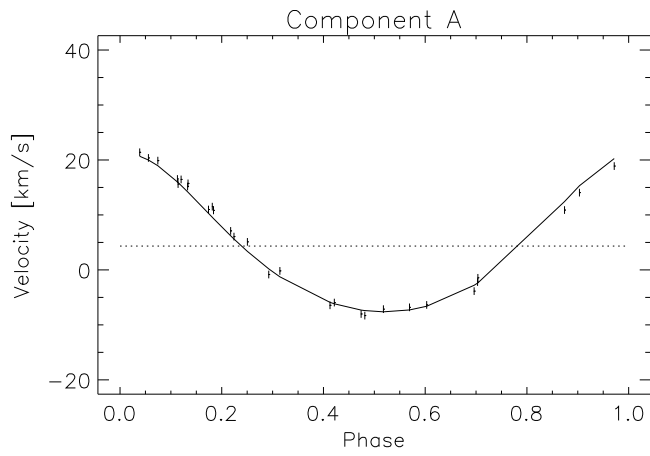


Fig. 13.— Spectroscopic orbit of the primary of Matar, with the fit.

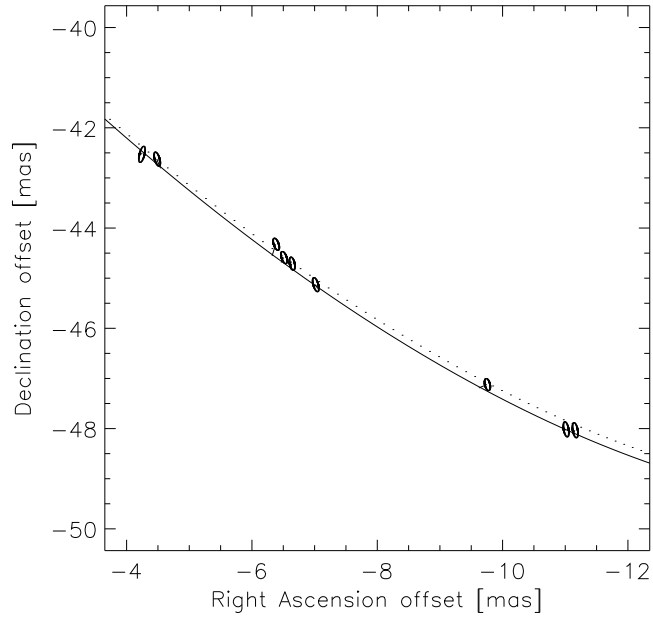


Fig. 14.— Apparent interferometric orbit of Matar. Detail showing NPOI data. The dotted line is the preliminary orbit published by Hummel & Armstrong (1992) based on Mark III data.

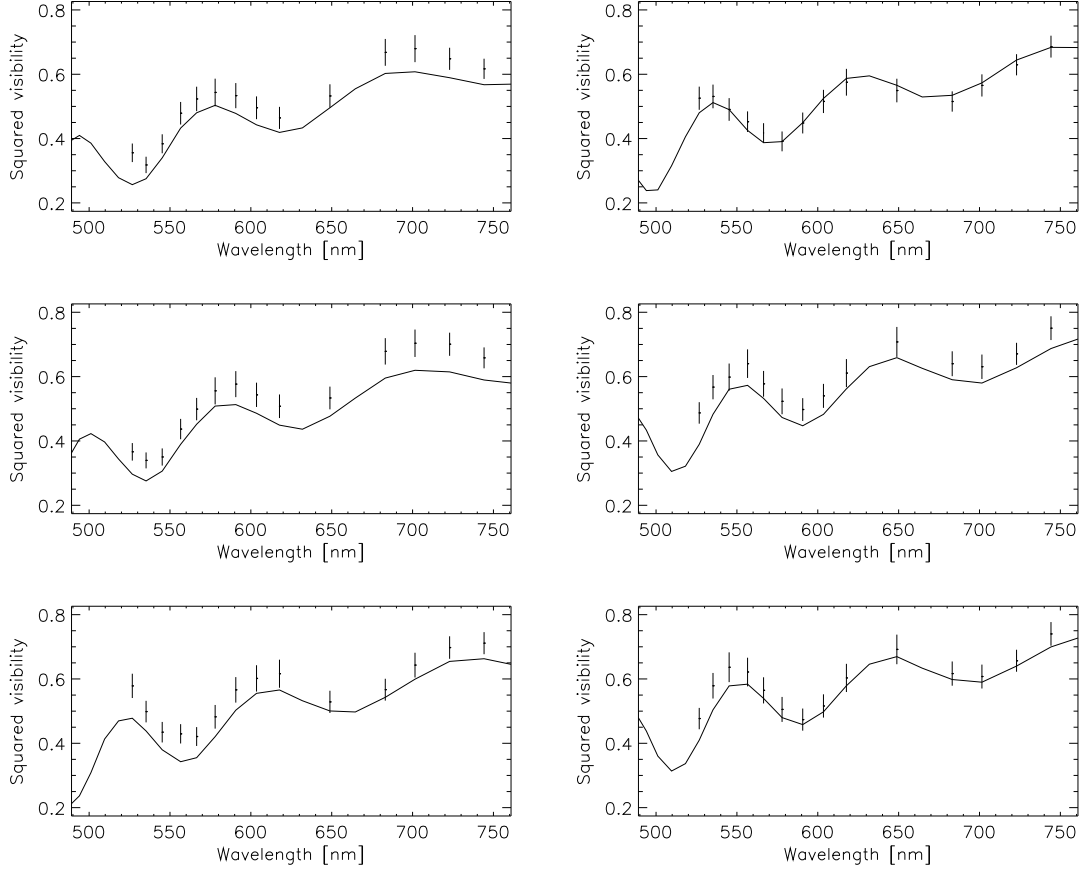


Fig. 15.— Squared visibility amplitude of Matar on the CW baseline versus wavelength for October 17, 1997, between 6 UT and 8.5 UT. Six scans are shown. Solid lines are model values based on parameters in Table 4.

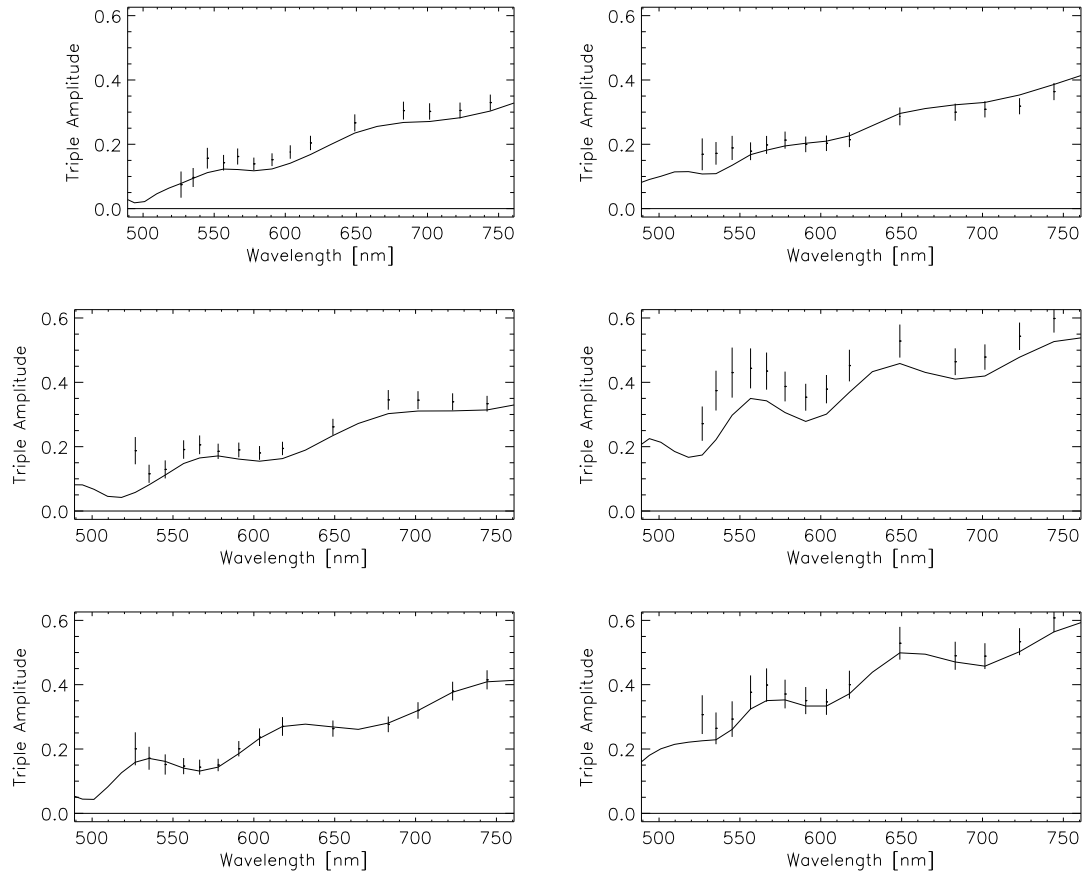


Fig. 16.— Triple amplitude of Matar versus wavelength for October 17, 1997. Six scans are shown. Solid lines are model values based on parameters in Table 4.

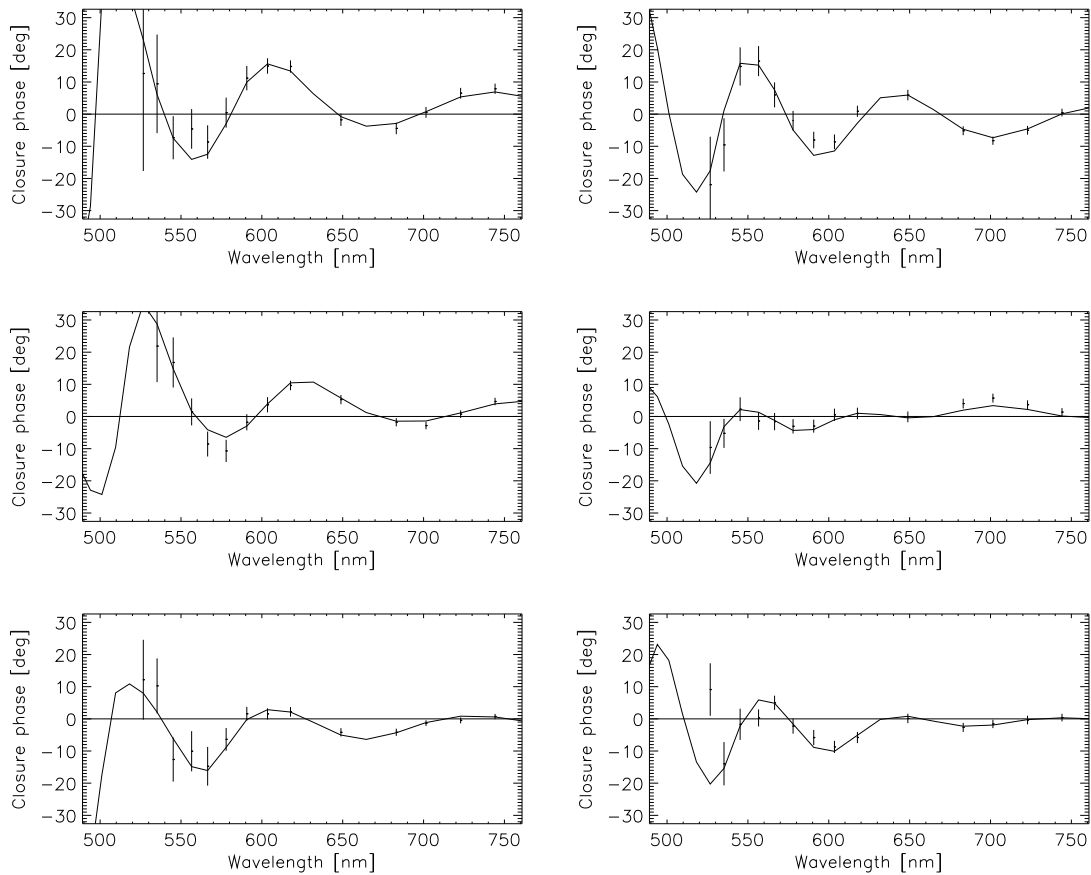


Fig. 17.— Closure phase (in degrees) of Matar versus wavelength for October 17, 1997. Six scans are shown. Solid lines are model values based on parameters in Table 4.

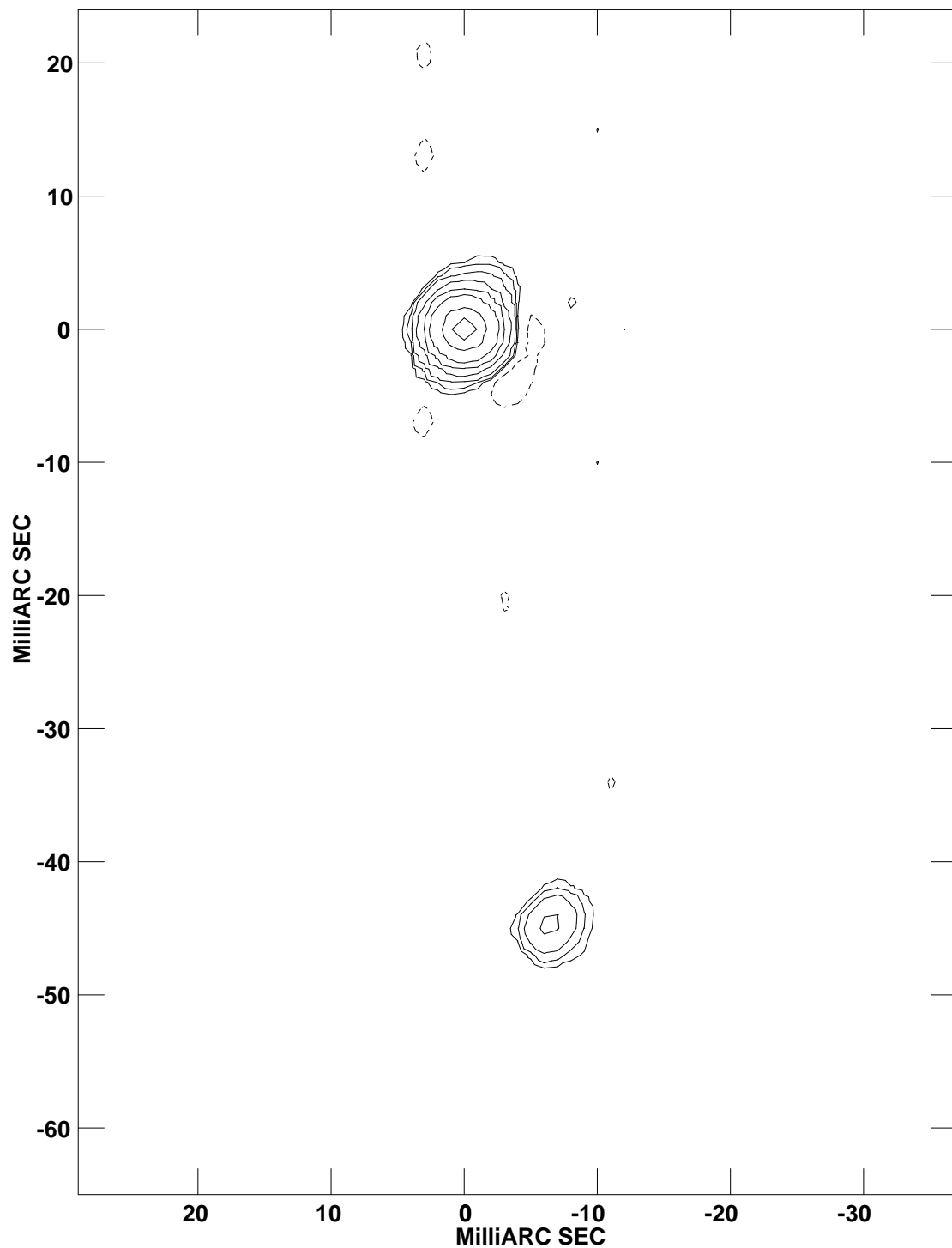


Fig. 18.— Image of Matar for October 17, 1997. Contours (in percent of peak): -0.5 , 0.5 , 1 , 2 , 5 , 10 , 20 , 50 , 80 . North is up, east to the left. Restoring beam is circular and 3 mas in diameter. Synthesized beam (point spread function) size is 4.8 mas by 1.9 mas, position angle -17° . The slight elongation of the components is probably an artefact resulting from the elongation of the synthesized beam. Note that the orientation of the binary has been determined unambiguously since NPOI measures the closure phases.